Journal of Low Temperature Physics
https://doi.org/10.1007/s10909-024-03104-2

Indium Bump Bonding: Advanced Integration Techniques for Low-Temperature Detectors and Readout

T. J. Lucas[1] · J. P. Biesecker[1] · W. B. Doriese[1] · S. M. Duff[1] · M. S. Durkin[1,2] · R. A. Lew[1,3] · J. N. Ullom[1,2] · M. R. Vissers[1] · D. R. Schmidt[1]

Received: 23 October 2023 / Accepted: 1 April 2024

Abstract
We have examined the influence of bump shape and bonding pressure on low-temperature electrical properties of indium bump connections including superconducting transition temperature, normal state resistance, and superconducting critical current. We describe our test structures, bonding process, and methods of characterization. At temperatures below 1 K, we observe critical currents greater than 70 mA for indium bump connections with a nominal bump size of 17 μm × 17 μm.

Keywords Hybridization · Indium bumps · Die bonding

1 Introduction

Indium bump bonding is an ideal process for the hybridization of low-temperature detector assemblies. Indium, a superconductor that remains ductile at low temperatures, can be fabricated into bumps at the wafer scale. Successful bolometer-based instruments such as SCUBA-2 [1] and HAWC+ [2] are demonstrations of large-scale integration of transition-edge sensor arrays and SQUID readout arrays with indium bump bonding. In this work, we examine the impact of compression and bump geometry on bump bond normal state resistance and critical current, I_C.

✉ T. J. Lucas
tammy.lucas@nist.gov

1 National Institute of Standards and Technology, Boulder, CO 80305, USA

2 University of Colorado, Boulder, CO 80309, USA

3 Theiss Research, La Jolla, CA 92037, USA

Published online: 20 April 2024

2 Test Structures

We previously described a three-layer bump process that can be integrated with our existing detector and readout processes [3]. The three layers consist of a niobium wiring layer, a titanium nitride under-bump metal, and the indium bump metal. For this work, we fabricated test structures in which the three layers had thicknesses of 200 nm, 150 nm, and 10 µm, respectively. The substrate was a 150 mm diameter Si wafer that was 0.5 mm thick, double side polished and had 150 nm of thermal oxide to serve as an etch stop and insulating layer.

The test structures consist of two different 13 mm × 17 mm chips that may be co-fabricated on the same wafer. Figure 1a illustrates how the 'base' and 'top' chips are bonded together. We can produce 50 chips per 150 mm wafer. The base chip has pads that can be used for both room temperature and low-temperature electrical measurements. The top chip is bonded to the base chip with a 90-degree rotation. Alignment verniers with 0.5 µm minor increments are in all four corners of the 10 mm × 10 mm bonding region. Bonding results in 4,182 bump connections with wiring that allows series measurement of bump chains containing between 2 and 102 bumps. Two bump form factors were fabricated on the same wafer, 17 µm × 17 µm square bumps, and 17 µm × 30 µm rectangular bumps that are rotated when bonding to form a cross.

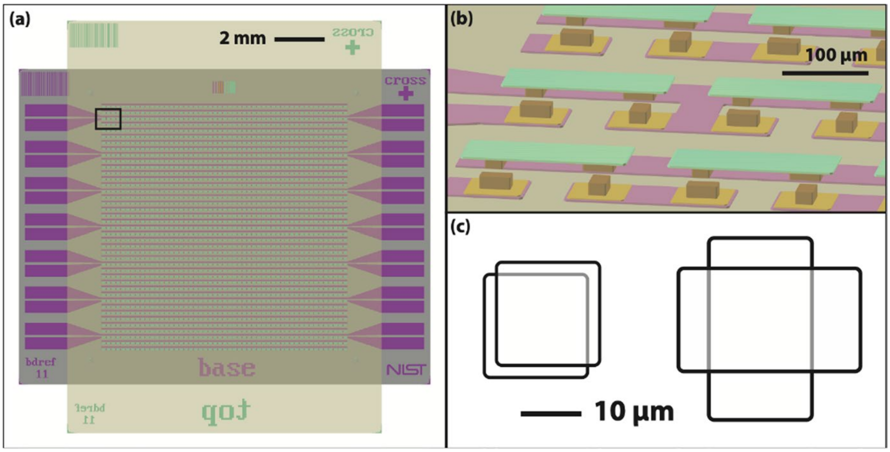

Fig. 1 (color online) **a** Test structure design. The top chip, *transparent*, is shown placed over the base chip. Both chips are 13 mm × 17 mm with a 10 mm × 10 mm bump field. Pads for electrical measurements are visible on the base chip. **b** Close up 3-dimensional rendering of the design region in the box shown in (**a**). Here, rectangular 17 µm × 30 µm bumps (brown) on the two chips are shown with a small separation. The wiring traces on the base chip (purple) can be used to probe series chains of bumps with the total number of bumps set by the pads used. **c** Illustration of the two bump form factors studied. The square and crossed rectangular bumps are each shown with a small misalignment

3 Bonding Process

The finished wafer is coated with a protective layer of photoresist and cut into chips with a dicing saw. Solvents are used for photoresist removal. The chips are inspected optically for any particles that might interfere with the bonding process. Indium forms a native oxide when exposed to air that may interfere with the bond. A surface treatment may be used to minimize the oxide impact [4], however the hydrogen products in this treatment can degrade the superconductivity of Nb-based devices [5, 6]. For this reason, in this work, we show results without any indium bump surface treatment.

The top chip is flipped into a custom machined chip cassette while protecting the indium. The cassette is placed into the die bonder. A tool with vacuum grooves suspends the chip bump side down. The tool has a 12 mm square pedestal such that the bonding region is supported, but the tool does not contact the edges of the 13 mm × 17 mm chip. The base chip is placed on a substrate tool via tweezers, where it is also held in place by vacuum grooves. Optical alignment is used to register the two chips using two sets of verniers in opposite corners. Typical pre-bond alignment is + / − 0.5 µm in the lateral dimensions. The pitch and roll of the top chip are adjusted to achieve a pre-bond parallelism of better than 100 micro-radians. After alignment and parallelism adjustments, the top chip is brought into contact with the base chip. The bonder is programmed to deliver a force profile in time defined by a piece-wise parabola-like function. Here, all bonding was conducted at room temperature with a force range from 1.5 kg to 6 kg.

Post-bond alignment is determined with infrared microscopy of the verniers. White light spectrometry of the air gap between the two chips is used to determine post-bond planarity and the final compressed thickness, t_f, of the bumps. Typical post-bond alignment is + / − 2 µm, and the air gap varies by + / − 1 µm across the 10 mm × 10 mm bonding region. The compression is defined by the expression $(t_i - t_f)/t_i$, where t_i is the initial thickness. The bump area and t_i are determined by laser scanning optical microscopy.

4 Results

Three sets of chips from the same wafer with both square and rectangular bumps were bonded, inspected, and subjected to low-temperature electrical testing. Figure 2a shows the measured compression as a function of bond force for both varieties of bumps. The bumps have a truncated pyramid shape that reduces the area at the top of the bump compared to the lithographically defined area as shown in the inset of Fig. 2b for a 17 µm × 30 µm bump. We determined using laser scanning profilometry that the total bonding area at contact is 0.08 mm^2 for square bumps and 0.20 mm^2 for rectangular bumps. Using these areas to calculate a bonding pressure result in the single curve shown in Fig. 2b.

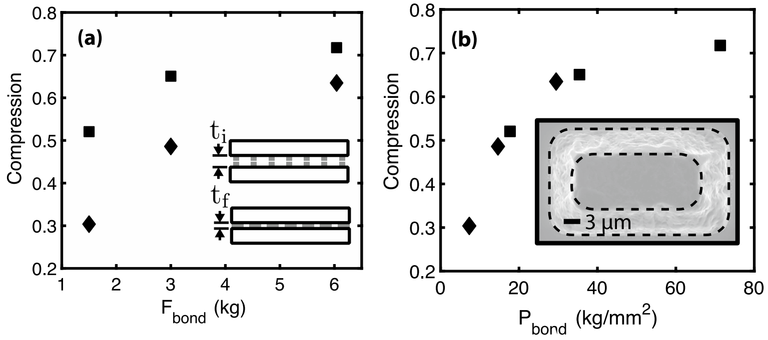

Fig. 2 **a** Bump compression after bonding. Squares show the measured compression as a function of bond force for the nominal 17 μm × 17 μm square bumps. Diamonds show the measured compression as a function of bond force for the nominal 17 μm × 30 μm rectangular bumps which are bonded to form a cross. Inset: the initial thickness, t_i, of the bumps is compressed to a final thickness, t_f, during bonding. **b** Measurements of the actual pre-bond area for each bump variant are used to determine a bonding pressure. Plotted as a function of pressure, the data from (**a**) fall on a single curve. Inset: SEM micrograph of 17 μm × 30 μm rectangular bump that illustrates (dashed lines) that the area of the top of the bump is less than the lithographically defined area

The bonded sets were mounted on printed circuit boards and Al wire bonded to four-wire pad configurations. In this work, we selected configurations that were 102, 70, or 24 bumps in series. The circuit boards were placed into a copper sample box and mounted to a two-stage adiabatic demagnetization refrigerator for measurements at temperatures down to 0.1 K. A low noise resistance bridge was used to measure the resistance as a function of temperature using

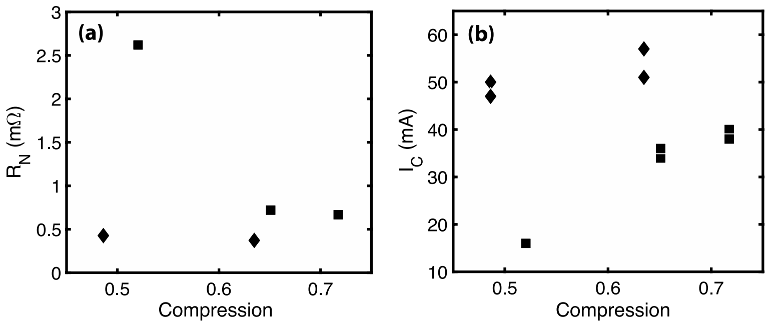

Fig. 3 **a** Per bump normal state resistance, R_N, of chains with 70 bump connections in series between 4.4 K and 4.5 K as a function of measured compression. The per bump resistance determined from chains with 24 and 102 bump connections are within 2% of the values shown. The 17 μm × 30 μm rectangular crossed bumps (diamonds) show a weaker dependence on compression than the 17 μm × 17 μm square bumps (squares). The lowest compression device from Fig. 1 exhibited a poor connection with high resistance and was not measured at low temperatures **b** Superconducting critical current as a function of measured compression at 2.9 K. For the same compression, the 17 μm × 30 μm rectangular crossed bumps (diamonds) have higher critical currents than 17 μm × 17 μm square bumps (squares) due to the geometrical difference of the cross-sectional area for current flow. While the lowest I_C device was not measured at lower temperatures, all other devices had I_C > 70 mA below 1 K

a current excitation of 10 μA. The superconducting transition temperature was 3.4 K for both square and crossed bumps. The per bump R_N, shown in Fig. 3a, was extracted from the average resistance measured with a resistance bridge between 4.4 K and 4.5 K divided by the number of bumps. Geometric arguments may explain the trends observed. The data suggests that an initial amount of compression is required to break through the indium oxide. As the square bumps are further compressed, conservation of the bump volume causes both the cross-sectional area for current flow to increase and the bump thickness to decrease. For the crossed rectangular bumps, the area and thickness are largely independent of compression. The critical current, I_C, was extracted from current–voltage characteristics measured using a current pulse with a duration of 10 ms at a low duty cycle to limit heating [7]. In Fig. 3b, we show the measured I_C for bonded sets at a temperature of 2.9 K. Similar geometric arguments may explain the trends. The maximum I_C that we could observe was 70 mA corresponding to the I_C of the Nb wiring. Below 1 K, the bump I_C may exceed that of the Nb wiring, and the measurement can only indicate that I_C is greater than 70 mA.

5 Conclusions

We have characterized our indium bump bonding process using a series of test structures with both square and crossed rectangular bump connections. Both form factors can produce high-quality superconducting connections. If spatial constraints allow the use of crossed rectangular bumps, they have the advantages of lower R_N and higher I_C with similar bonding force while also potentially having a higher misalignment tolerance. The bump bonds described here are suitable for a range of applications with either one bump per connection or a small number in parallel. Instruments based on transition-edge sensors typically have circuits that are required to carry up to 10 mA of current [8] while metallic magnetic calorimeter circuitry may require 100 mA of current [9]. While we continue to explore the parameter space of bump form factor and bonding parameters, the processes described here have been successfully applied to a demonstration of bump bonded superconducting readout for x-ray transition-edge sensors [10]. Future work will include applying this type of characterization to different thicknesses of bumps and single-sided bumps with indium on one side.

Acknowledgements We gratefully acknowledge support from the NIST Scalable Superconducting Computing and NASA Goddard Space Flight Center ATHENA projects.

Author contributions TJL, JPB, and DRS wrote the main manuscript text, JPB analyzed the data, and DRS prepared the figures. All authors reviewed the manuscript and significantly contributed to this work.

Data Availability Data generated and/or analyzed during this study are available from the corresponding author on reasonable request.

Declarations

Competing interests The authors declare no competing interests.

References

1. D.A. Harper et al., HAWC+, the far-infrared camera and polarimeter for SOFIA. J. Astron. Instrum. **07**(04), 1840008 (2018). https://doi.org/10.1142/S2251171718400081
2. W.S. Holland et al., SCUBA-2: the 10,000 pixel bolometer camera on the James Clerk Maxwell Telescope. Mon. Not. R. Astron. Soc., **430**, 2513–2533 (2013). https://doi.org/10.1093/mnras/sts612
3. T.J. Lucas et al., Indium bump process for low-temperature detectors and readout. J. Low Temp. Phys. (2022). https://doi.org/10.1007/s10909-022-02728-6
4. E.F. Schulte, K.A. Cooper, M. Phillips, S.L. Shinde, "Characterization of a novel fluxless surface preparation process for die interconnect bonding,", IEEE 62nd Electronic Components and Technology Conference. San Diego, CA, USA **2012**, 26–30 (2012). https://doi.org/10.1109/ECTC.2012.6248801
5. K. Hinode et al., Hydrogen-inclusion-induced critical current deviation of Nb/AlOx/Nb Josephson junctions in superconducting integrated circuits. IEEE Trans. Appl. Supercond. **19**(3), 131–134 (2009)
6. D. Amparo et al., "Investigation of the role of H in fabrication-process-induced variations of Nb/Al/AlO_x/Nb Josephson junctions," IEEE Trans. Appl. Supercond., **21**(3) (2011)
7. B. Foxen et al., Quantum Sci. Technol. **3**, 014005 (2018). https://doi.org/10.1088/2058-9565/aa94fc
8. K. Irwin, G. Hilton, Transition-Edge Sensors. In: C. Enss, (eds) Cryogenic Particle Detection. Topics in Applied Physics, vol 99. Springer, Berlin, Heidelberg. https://doi.org/10.1007/10933596_3
9. A. Fleischmann, C. Enss, G. Seidel, Metallic magnetic calorimeters. In: Enss, C. (eds) Cryogenic Particle Detection. Topics in Applied Physics, vol 99. Springer, Berlin, Heidelberg. https://doi.org/10.1007/10933596_4
10. M. Durkin et al., Symmetric time-division-multiplexed SQUID readout with two-layer switches for future TES observatories. IEEE Trans. Appl. Supercond. **33**(5), 1–5 (2023). https://doi.org/10.0009/TASC.2023.3264175